Measurements of partial cross sections and photoelectron angular distributions for the photodetachment of Fe^- and Cu^- at visible photon wavelengths

A. M. Covington,* Srividya S. Duvvuri, E. D. Emmons, R. G. Kraus, W. W. Williams, and J. S. Thompson
Department of Physics and Nevada Terawatt Facility, MS 220, University of Nevada, Reno, Nevada 89557-0058, USA

D. Calabrese
Department of Physics, Sierra College, Rocklin, California 95677, USA

D. L. Carpenter
National Renewable Energy Laboratory, Golden, Colorado 80401-3393, USA

R. D. Collier
Department of Physics, Western Nevada Community College, Carson City, Nevada 89703, USA

T. J. Kvale
Department of Physics and Astronomy, The University of Toledo, Toledo, Ohio 43606-3390, USA

V. T. Davis
Test Support Division, Defense Threat Reduction Agency, West Desert Test Center, Dugway, Utah 84022-5000, USA
(Received 6 September 2006; revised manuscript received 26 October 2006)

Photodetachment cross sections and the angular distributions of photoelectrons produced by the single-photon detachment of the transition metal negative ions Fe^- and Cu^- have been measured at four discrete photon wavelengths ranging from 457.9 to 647.1 nm (2.71–1.92 eV) using a crossed-beams laser photodetachment electron spectrometry (LPES) apparatus. Photodetachment cross sections were determined by comparing the photoelectron yields from the photodetachment of Fe^- to those of Cu^- and C^-, which have known absolute photodetachment cross sections. Using the measured photodetachment cross sections, radiative electron attachment cross sections were calculated using the principle of detailed balance. Angular distributions were determined by measurements of laboratory frame, angle-, and energy-resolved photoelectrons as a function of the angle between the linear laser polarization vector and the momentum vector of the collected photoelectrons. Values of the asymmetry parameter have been determined by nonlinear least-squares fits to these angular distributions. The measured asymmetry parameters are compared to predictions of photodetachment models including Cooper and Zare's dipole approximation theory [J. Cooper and R. N. Zare, J. Chem. Phys. **48**, 942 (1968)], and the angular momentum transfer theory developed by Fano and Dill [Phys. Rev. A **6**, 185 (1972)].

DOI: XXXX PACS number(s): 32.80.Gc, 32.10.−f, 32.80.Cy, 33.60.−q

I. INTRODUCTION

Atomic negative ions play important roles in many laboratory and astrophysical plasmas. In plasma environments where electron temperatures are of the order of the electron affinities of atoms, detailed cross sections are necessary for understanding processes that lead to the formation and destruction of negative ions [1]. For Cu^-, processes such as photodetachment and radiative electron attachment can play important roles in determining population inversions in copper-vapor lasers (CVL) [2]. Moreover, theoretical investigations suggest that transition metal anions, such as Fe^-, may act as intermediaries in the formation of molecules in astrophysical objects such as class II supernovas [3]. For instance, unidentified features in the infrared spectrum of SN1987A taken on day 192 have been ascribed to the FeO molecule, which is formed from cosmically abundant elements. It has been proposed that the formation of these molecules may come about through stimulated radiative attachment via the following reaction [3],

$$\mathrm{Fe} + \mathrm{e}^- + h\nu \rightarrow \mathrm{Fe}^- + h\nu + h\nu, \tag{1}$$

which is followed by an associative reaction of the form,

$$\mathrm{Fe}^- + \mathrm{O} \rightarrow \mathrm{FeO} + e^-. \tag{2}$$

Although these reactions have been hypothesized to be important, no experimental data exists for the radiative attachment (RA) cross sections needed to accurately calculate the rates in the process described in Eq. (1) above. Fortunately, since radiative electron attachment is the inverse process of photodetachment, the principle of detailed balance can be used to convert photodetachment (PD) cross sections into corresponding radiative attachment cross sections.

In order to accurately measure the relative photodetachment cross sections and set them on an absolute scale, well-characterized measurements of the photoelectron angular distributions and photoelectron yields were necessary for Fe^-

*Electronic address: aaron@physics.unr.edu

and the reference ions, C^- and Cu^-. Photodetachment cross sections for C^- [4,5] and Cu^- [6] are already known, and hence the ratio of normalized photoelectron yields for the reference ions could be used to benchmark the experimental technique and calibrate the Fe^- cross section data. The measurements presented in this paper are applied to these ends.

A wealth of information can be found in the literature pertaining to binding energies in atomic negative ions and the breadth of the field is illustrated in reviews compiled by Andersen *et al.* [7] and Rienstra-Kiracofe *et al.* [8]. In contrast to electron affinities, there exists a relative paucity of experimental data for collision processes involving negative ions. Cross section measurements are rare for processes such as photodetachment and radiative electron attachment. Moreover, relatively few measurements of photoelectron angular distributions are available for transition metal negative ions [9,10]. Summaries of previous photon-anion collision studies are given in recent reviews by Andersen [11] and Pegg [12]. Further laboratory measurements of these processes are needed to elucidate the contributions of these species to astrophysical plasma environments.

Photodetachment studies can be used to probe the fundamental structure of atomic anions. Moreover, the photodetachment process is a bound-free transition which provides a unique opportunity to examine electrons leaving a neutral atomic core in the presence of short-ranged potentials [1]. Therefore, subtle interactions such as electron correlation and relativistic effects can be investigated in photodetachment studies. These effects may be veiled by the long-range Coulomb potential present in the photoionization of either neutral or positively charged ionic species.

In total photodetachment cross-section calculations, quantities such as the magnitude and relative phases of transition amplitudes are usually integrated over. In contrast, differential cross-section calculations depend explicitly on these quantities. Hence, differential cross-section calculations can be used to obtain both the yield and angular distributions of photoelectrons. The most general form of the angular distribution of a collision process for an unpolarized target can be summarized in the theorem derived by Yang [13]: "If only incoming waves of orbital angular momentum L contribute appreciably to the reaction, the angular distribution of the outgoing particles in the center of mass system is an even polynomial of cos θ with maximum exponent not higher than $2L$." Here θ is the angle between the incoming and outgoing particles in the center-of-mass system. It should be noted that the angular distribution does not contain a term linear in cos θ since parity is conserved in a photoabsorption process. In the theory developed by Cooper and Zare [14] as applied to the single-photon detachment of negative ions, the differential cross section for the production of photoelectrons detached from a randomly polarized target (i.e., a statistical population of all degenerate states) by incident linearly polarized light, can be written in the dipole approximation as

$$\frac{d\sigma}{d\Omega} = \frac{\sigma}{4\pi}\left(1 + \frac{\beta}{2}(3\cos^2\theta - 1)\right), \tag{3}$$

wherein σ is the total photodetachment cross section at a given photon energy, β is the asymmetry parameter, and θ is the angle between the photon polarization vector and photodetached electrons in the center-of-mass system. The asymmetry parameter completely characterizes the shape of the photoelectron emission pattern, and in order for the differential cross section to be non-negative, the values of β are restricted to the range $-1 \leq \beta \leq 2$. Within the independent-particle approximation, the asymmetry parameter for the photoejection of an electron from an initial state with angular momentum l_o is given by [15]

$$\beta = \frac{l_o(l_o-1)R^2_{l_o-1} + (l_o+1)(l_o+2)R^2_{l_o+1} - 6l_o(l_o+1)R_{l_o+1}R_{l_o-1}\cos(\delta_{l_o+1} - \delta_{l_o-1})}{(2l_o+1)[l_oR^2_{l_o-1} + (l_o+1)R^2_{l_o+1}]}. \tag{4}$$

The asymmetry parameter is found to be most sensitive to the phase shift differences $\delta_{l_o+1} - \delta_{l_o-1}$, though it is also dependent upon the relative magnitudes of the radial dipole integrals R_{l_o+1} and R_{l_o-1}.

Spectral variations of photoelectron angular distributions in the vicinity of resonances [16] have been predicted to depart markedly from those of direct (nonresonant) photoprocesses such as those in the model of Cooper and Zare. The energy dependence of the asymmetry parameter in this case is due to a configuration interaction, which allows alternative final-state channels for the liberated photoelectron. Spectral variation of the asymmetry parameter may also be enhanced near cross-section minima, due to rapid changes in the relative magnitudes of the amplitudes for the various channels [17].

A more detailed theoretical description of the photodetachment process must also consider the final-state interaction between the photoelectron and its parent residual atom. The coupling of the outgoing electron partial waves to the residual atom can result in various photodetachment channels, which can be described by a single-photon process of the form,

$$A^-(L_o,S_o,J_o,\pi_o) + \gamma(j_\gamma = 1, \pi_\gamma = -1) \rightarrow A(L_c,S_c,J_c,\pi_c) + e^-(l,s,j,\pi_e = (-1)^l), \tag{5}$$

wherein, S_o, L_o, and J_o are the spin, orbital, and total angular momentum quantum numbers, respectively, of the initial ion (A^-) states. Similarly, S_c, L_c, and J_c are the spin, orbital, and total angular momentum quantum numbers of the final state

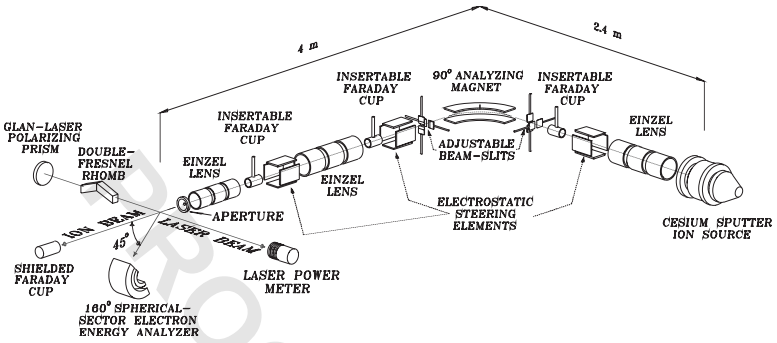

FIG. 1. Laser photodetachment electron spectroscopy (LPES) experimental apparatus.

neutral core (A), and l,j are the orbital and total angular momentum quantum numbers for the photoelectron. Using the angular momentum transfer theory formalism of Fano and Dill [18], this coupling produces allowed angular momentum transfers from the photon to the ion expressed by $\boldsymbol{j}_t=\boldsymbol{L}_c-\boldsymbol{L}_o$. Here $\boldsymbol{L}_c$ and $\boldsymbol{L}_o$ are the orbital angular momenta of the daughter residual atomic core and parent negative ion, respectively. Within the electric dipole and LS-coupling approximations, parity conservation assigns values which are either parity favored $[\pi_o\pi_c=(-1)^{j_t}]$ or unfavored $[\pi_o\pi_c=(-1)^{j_t+1}]$. Within this formalism, the effective value of the asymmetry parameter β can be written as a weighted average of the form,

$$\beta=\frac{\sum_{j_t}\sigma(j_t)\beta(j_t)}{\sum_{j_t}\sigma(j_t)}. \quad (6)$$

In this equation, the summation extends over all allowed values of j_t. In Eq. (6), $\beta(j_t)$ and $\sigma(j_t)$ are the asymmetry parameters and partial photodetachment cross sections characteristic of a given value of j_t. Both the photodetachment cross sections and asymmetry parameters can be expressed in terms of scattering amplitudes $S_l(j_t)$, where l is the orbital angular momentum of the photoelectron, and is restricted to the values $j_t\pm1$ or j_t [15].

II. EXPERIMENTAL APPARATUS AND PARAMETERS

A schematic diagram of the experimental apparatus is shown in Fig. 1. More detailed descriptions of the operation of the cesium-sputter-type negative ion source [19,20] and laser photodetachment electron spectroscopy (LPES) apparatus have been given previously [21,22], so only a synopsis of these are given here. For all measurements, the Fe^- and Cu^- negative ion beams were produced with a sputter target containing a composition by mass of 70% iron, 20% copper, and 10% carbon graphite powders pressed into a solid sputter pellet. Positively charged cesium ions were accelerated to kinetic energies ranging from 2–6 keV towards the negatively-biased, cesium-coated pellet. The sputtering acceleration-voltage was adjusted until optimal negative ion beam currents were extracted from the source. As the negative ions exited the extraction region, they were accelerated to a kinetic energy of 10 keV. The typical operational pressure in the ion source region was 2.7×10^{-5} Pa.

Following extraction from the ion source, the negative ion beam was focused and momentum analyzed using a postacceleration, 90° bending magnet with a mass resolution of 200. This arrangement permitted the selection of isotopically pure negative ion beams for photodetachment studies. Two-dimensional, adjustable beam slits were used at the entrance and exit foci of the magnet to spatially confine the transverse extent of the ion beam. The mass-selected ion beam was focused with a second pair of Einzel lenses, and collimated with apertures before entering the experimental chamber. The post magnet section of beam line was differentially pumped to a pressure of 4×10^{-7} Pa. These vacuum levels were maintained in order to minimize degradation of the ion beam through collisional detachment processes. After entering the chamber, the ion beam was crossed by a laser-produced, linearly polarized photon beam at an intersection angle of 90°. Upon reaching the interaction region, the ions had traveled a total distance of 6.4 m. Typical pressures in the interaction region were maintained near 1×10^{-6} Pa to reduce background electron counts.

The photon beams (457.9, 476.5, 488.0, and 514.5 nm) were produced by either a 25 W Coherent® Model Sabre R or a 5 W Spectra Physics® Model 2045 argon-ion laser operating in single line mode. Red light (647.1 nm) was generated with a 1 W Spectra Physics® Model 2030 krypton-ion laser operating in multiline mode. An external prism was used for wavelength selection for the krypton-ion laser. Rotation of the linear polarization vector about the photon beam axis was accomplished through the use of a λ/2-phase retarder (double-Fresnel rhomb or half-wave plate) mounted in a micrometer-driven rotational stage. The output power level of the laser was monitored with a power meter, and the ion beam current was collected in a shielded Faraday cup. Both signals were continuously monitored and recorded for normalization of the photoelectron data.

Electrons photodetached in the interaction region were energy analyzed using a spherical-sector, 160° electrostatic kinetic energy analyzer operated in a fixed pass-energy mode. The analyzer was operated with a pass energy of 20 eV for the measurements presented here. The symmetry axis of the electron spectrometer is bisected by the plane which contains the velocity vector of the ion beam and is orthogonal to the photon beam propagation vector. The spectrometer is mounted in a goniometric cradle, and can be rotated from a 45°–90° declination angle with respect to the ion beam axis in order to facilitate systematic studies of kinematic effects. For all the measurements presented in this

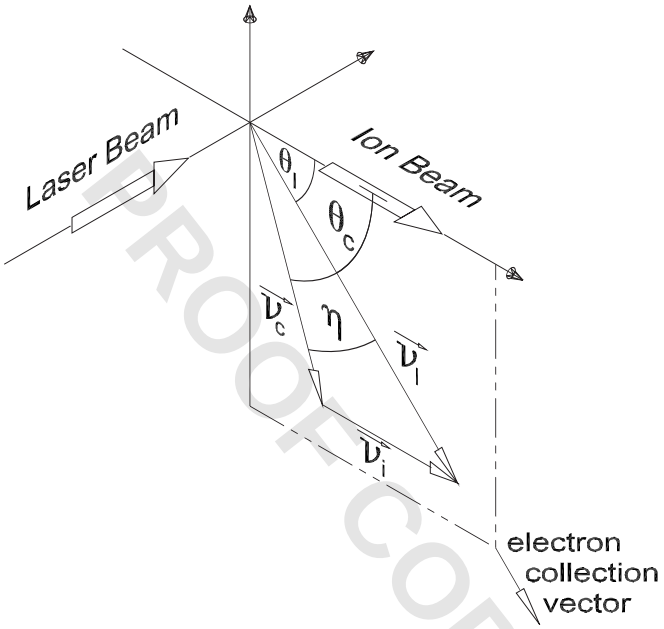

FIG. 2. Kinematic transformation diagram for ion ($\vec{v_i}$), center-of-mass photoelectron ($\vec{v_c}$), and laboratory-frame photoelectron ($\vec{v_l}$), velocity vectors.

paper, the spectrometer was located at a 45° declination angle.

In this experiment, the orientation of the electron spectrometer requires kinematic adjustments to be made to the measured photoelectron energies. These adjustments correct for energy differences between the center of mass (ion) and the laboratory (rest) frames of reference. In the ion frame, the energy balance equation can be used to determine the center-of-mass electron kinetic energy $E_c = h\nu - E_{EA}$, where E_{EA} is the electron affinity of the atom. A transformation equation relating E_c with its corresponding energy in the laboratory frame E_l is given by [23]

$$E_c = E_l + \epsilon - 2\sqrt{\epsilon E_l}\cos\,\theta_l, \tag{7}$$

where $\epsilon = \frac{1}{2}m_e v_i^2$ is the kinetic energy of an electron moving with the same velocity v_i as an ion in the beam, and θ_l is the angle subtended between the electron's laboratory velocity vector and the velocity vector of an ion in the beam. Solving Eq. (7) for the laboratory energy yields two physical solutions corresponding to photoelectrons ejected in the forward (spectrometer) and backward directions. Only photoelectrons ejected with momentum vectors in the forward direction were detected in the $\theta_l = 45°$ declination angle geometry.

A velocity vector diagram illustrating these kinematic transformations is shown in Fig. 2. As an example calculation of kinematic transformations, consider the photodetachment of a 10.0 keV Cu^- beam ($v_i = 1.86 \times 10^7$ cm/s) with $\epsilon = 0.087$. For Cu, $E_{EA} \sim 1.23$ eV [24], so photodetachment with 2.41 eV (514.5 nm) photons gives $E_c \simeq 1.17$ eV ($v_c = 6.43 \times 10^7$ cm/s), and the lab frame energy is $E_l = 1.62$ eV ($v_l = 7.54 \times 10^7$ cm/s).

Also shown in Fig. 2 is the angular difference, $\eta = \theta_c - \theta_l$ between center of mass and laboratory angles for a given fast-moving ion. These angles are related by the following expression [23]:

$$\eta = \sin^{-1}\left(\frac{v_i}{v_c}\sin\,\theta_l\right). \tag{8}$$

In certain measurements, such as relative photodetachment cross sections, kinematic effects must also be included for the frame-transformed solid angle ratio, γ, which is given by [23],

$$\gamma = \sqrt{\frac{E_c}{E_l}}\left(1 - \sqrt{\frac{\epsilon}{E_l}}\cos\,\theta_l\right). \tag{9}$$

The relatively low laboratory frame electron energies (≤ 3 eV) required that care be taken to reduce the effects of stray electric and magnetic fields in the experimental chamber. Electrons with the correct energy for transmission through the spherical-sector analyzer were detected with a channel electron multiplier (CEM) operated in the particle-counting mode with a typical gain of 10^8. Detected electron pulses were amplified in succession by a preamplifier and amplifier. Following amplification, electron pulses entered a constant fraction discriminator (CFD) set to a discrimination level of 0.38 V to discriminate against electronic noise not associated with the photodetachment process. Signal pulses passing through the CFD were converted to +5 V transistor-transistor logic (TTL) pulses, and counted and logged by a PC based data acquisition and control system. The ion beam current and laser power were recorded for normalization of the electron counts.

Before each photoelectron kinetic energy spectrum was measured, the ion beam was focused and positioned for maximum beam transmission. A set of apertures placed 30 cm apart was used to collimate the ion beam to a diameter of 4 mm, and the laser was focused to a diameter of 1 mm in the interaction region with a lens. Thereafter, the overlap between the photon and ion beams was optimized through the following procedure: (i) signal maximization at the peak of the photoelectron spectrum was obtained by rastering the photon beam through the ion beam, (ii) once maximum signal yield was obtained, the photon polarization vector was rotated through 180° (at which point the signal yield should reproduce what was obtained in the previous step), and the same procedure was carried out again. Through iteration, the maximum signal yield was obtained at both ends of the scan spectrum while monitoring the laser power through the interaction to ensure that the laser was normally incident to the surfaces of the $\lambda/2$-phase retarder. A starting position was established by determining the polarizer angle for maximum photoelectron yield. Thereafter, measurements were made every 10° over a total range of 240°. The photoelectron and normalization signals were carefully monitored to avoid saturating the photodetachment process or charged particle detection electronics during the experiments. The saturation levels were determined with diagnostic measurements of photoelectron signal as a function of laser power.

III. MEASUREMENTS AND ANALYSIS

A. Data acquisition and analysis techniques

The specific experimental techniques used to measure photodetachment cross sections and photoelectron angular distributions for transition metal negative ions are described in this section. Ion and laser beam stabilities during these measurements were better than 98%. Signal-to-noise ratios were typically 100:1 near the peaks of the angular distribution scans. The electron spectrometer pass energy for these measurements was 20 eV, and each scan was made over a 1.0 eV lab energy range. This energy range was usually divided into 100 equal steps, each having an integration time of 2 seconds.

Following collection, each of the photoelectron spectra were fitted to the superposition of a Gaussian function with a linear background that used a nonlinear, least-squares fitting routine that weighted each individual data point by its statistical uncertainty assuming a Poisson distribution. Once the fitting parameters were obtained, each Gaussian function was integrated in order to determine the total photoelectron yield along with its uncertainty at each indicated angle of the $\lambda/2$-phase retarder, which corresponds to the angle between the laser polarization vector and the electron collection direction. After determining the yields and uncertainties of each of the individual spectra, the asymmetry parameter was determined by a least-squares fit of photoelectron yield-vs-linear polarization angle with respect to electron collection direction data to the general expression: $I(\theta)=a[1+\beta P_2(\cos(\alpha-c))]$, where $P_2(\cos(\alpha-c))$ is the second order Legendre polynomial, and a, β, and c are fitting parameters. The angle, c, was used to establish the absolute angle, θ, given in Eq. (3) for an ion with known asymmetry parameter, and α is the step angle of these measurements. Details of the procedure used to determine the absolute angle have been discussed previously [10]. Experimental uncertainties for all angular distribution measurements include statistical and estimated systematic errors summed in quadrature as discussed below.

A Poisson distribution was assumed for counting statistics of each individual data point on each photoelectron spectrum. Consequently, the counting statistics of each photoelectron spectrum were reflected in the uncertainties in the Gaussian fitting parameters. Uncertainties in the Gaussian fitting parameters, in turn, provided upper and lower bounds in the subsequent integrations to determine the photoelectron yield at each polarization angle. Following integration, uncertainties in the photoelectron yields were propagated to uncertainties of the fits for the determination of the asymmetry parameter, and are included to within one standard deviation. Typically, the weighted mean of all fits at each wavelength deviated by less than 5%. At each laser wavelength, a minimum of three and maximum of five individual scans were needed to realize this convergence. Systematic errors for all angular distribution measurements are estimated to be less than 5%. These include contributions from time-dependent changes in the overlap of the ion and laser beams during the course of each scan, as well as practically achievable alignment constraints. Uncertainties in both the reproducibility of the laser polarization angle and depolarization of the laser beam were determined to be negligible in comparison to the previously mentioned alignment errors.

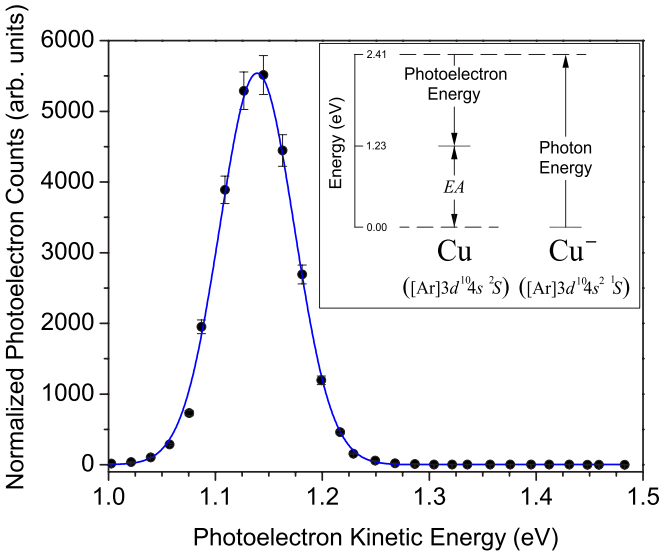

FIG. 3. (Color online) Typical center-of-mass photoelectron kinetic energy spectrum of $^{63}Cu^-$ measured at a polarization angle of 0° and a photon wavelength of 514.5 nm. The inset is a schematic energy level diagram for the photodetachment of Cu^-.

B. Angular distributions of Cu^-

The spectral dependence of the asymmetry parameter of Cu^- was determined by measuring photoelectron angular distributions at four discrete visible photon wavelengths (647.1, 514.5, 488.0, and 457.9 nm). The relative ^{63}Cu and ^{65}Cu negative ion beam intensities were 69.0±0.2:31.0±0.2. These intensities were in good agreement with the accepted relative abundances of 69.17(2):30.83(2) tabulated for stable copper isotopes [25]. Typical Cu^- ion beam currents ranged from 48–52 nA during all data scans, and laser power levels ranged from 0.35 W for the 647.1 nm to 8.25 W for the 514.5 nm wavelengths, respectively. A photoelectron kinetic energy spectrum following the photodetachment of Cu^- is shown in Fig. 3, along with a schematic energy level diagram for the photodetachment process. This spectrum can be described by the following single-photon, single-electron process: $h\nu+\mathrm{Cu}^-([\mathrm{Ar}]3d^{10}4s^{2}{}^1S)\rightarrow \mathrm{Cu}([\mathrm{Ar}]3d^{10}4s^{2}S)+e^-(kp)$, where kp identifies a continuum p-state electron. The electron affinity of Cu is defined as the difference in total electronic binding energies between the $^2S_{1/2}$ neutral atom and $^1S_0$ negative ion ground states, and has been previously determined to have a value of 1.23581(4) eV [24]. Hence, the center-of-mass photoelectron energies for the photodetachment of Cu^- ranged from 0.68 to 1.48 eV for these measurements.

A plot of a typical photoelectron yields (solid circles) as a function of polarization angle is given in Fig. 4 for Cu^- at a photon wavelength of 514.5 nm. Also shown in Fig. 4 is a nonlinear least-squares Gaussian fit of these data (solid curve). The experimentally determined values of the asym-

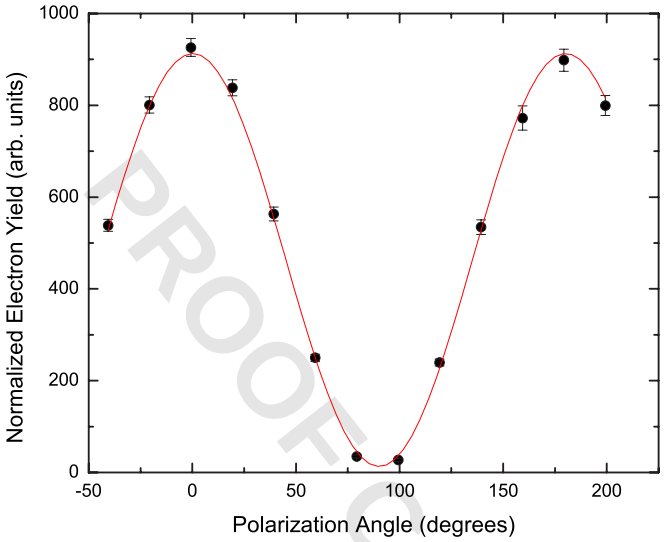

FIG. 4. (Color online) A plot of photoelectron yields as a function of polarization angle for $^{63}Cu^-$. These data were measured at a wavelength of 514.5 nm.

metry parameter for the single-photon detachment of Cu^- at all measured wavelengths (or photoelectron energies above threshold) are given in Table I, along with respective experimental uncertainties. Also shown in Table I is the experimentally determined value of the asymmetry parameter measured by Hotop *et al.* [26]. In this photoelectron energy regime, the energy independence (lack of spectral variation) of the asymmetry parameter for the photodetachment of Cu^- is demonstrated by the relatively constant β values in Table I.

The lack of spectral variation of the asymmetry parameter for Cu^- photodetachment is well described by the theory of Cooper and Zare [14]. This theory is valid so long as configuration interaction can be ignored in both the initial state anion and residual neutral core. For *s*-electron detachment at energies far from the photodetachment threshold, the value of the asymmetry parameter approaches $\beta=2$. This value is readily apparent if $l_o=0$ is substituted for the initial state angular momentum in Eq. (4) above. In general, the photodetachment of electrons from a subshell with initial orbital angular momentum l_o produces continuum electrons with orbital angular momenta $l_o\pm1$. However, within the framework of the independent electron approximation, the bound valence electron of Cu^- occupies an *s* subshell, which limits the final state description to a ^2S neutral atomic core and a *p*-wave continuum electron. In terms of angular momentum transfer theory [15], this limitation comes about when recognizing that the initial ionic parity π_o, and the final neutral parity π_c must be equivalent. Hence, parity favored values of the angular momentum transfer for the photodetachment of Cu^- limit the product of initial and final state parities such that $\pi_o\pi_c=(-1)^{l+1}=+1$, which implies that only odd values of l are allowed. Therefore, a single-photon detachment process results in a continuum electron with a single orbital angular momentum, $l=1$ (p wave). The experimental measurements confirm that the asymmetry parameter reduces to an energy independent value of $\beta=2$. Moreover, the photoelectron asymmetry parameters measured following the photodetachment of Cu^- are in excellent agreement with the predictions of both Cooper and Zare's model and the angular momentum transfer theory.

TABLE I. Asymmetry parameters for the single-photon detachment of Cu^- at visible photon wavelengths. Measured values of the asymmetry parameter are tabulated along with experimental error bars representing one standard deviation of the mean. The error bars represent contributions from fitting uncertainties summed in quadrature with estimated systematic errors. Within the experimental error, $\beta=2$ for each measurement as is expected for *s*-electron photodetachment. The asymmetry parameter β_{prev} was measured by Hotop *et al.* [26].

Photon wavelength λ (nm)	Photoelectron energy (eV)	Asymmetry parameter β_{prev}	Asymmetry parameter β_{exp}
647.1	0.682		$1.98^{+0.02}_{-0.03}$
514.5	1.182		1.97±0.03
488.0	1.312	2.00±0.03	1.96±0.03
457.9	1.480		$1.97^{+0.03}_{-0.04}$

C. Angular distributions of Fe^-

The spectral dependencies of the asymmetry parameters for the single-photon detachment of Fe^- were also investigated at four discrete visible photon wavelengths (647.1, 514.5, 488.0, and 457.9 nm). Laser power levels for measurements ranged from a minimum of 0.35 W for the 647.1 nm line to a maximum of 8.5 W for the 514.5 nm line. The signal-to-noise ratios approached 500:1 near the maximum of the angular distribution of the largest of the photopeaks because of the magnitudes of the ion beam current, laser power levels, and photodetachment cross section values.

The photodetachment of Fe^- to the neutral ground state of Fe can be described by the following single-photon, single-electron process: $h\nu+\text{Fe}^-([\text{Ar}]3d^74s^2\ ^4F)\rightarrow\text{Fe}([\text{Ar}]3d^64s^2\ ^5D)+e^-(kp,kf)$ and is illustrated in Fig. 5. The electron affinity of Fe is defined as the difference in total electronic binding energies between the $^5D_4$ neutral atom ground state and $^4F_{9/2}$ negative ion ground state, and has been previously measured to a value of 0.151(3) eV [27]. In addition, three alternative photodetachment channels are accessible for photon energies in excess of 1.92 eV from the ^4F negative ion state to excited states of the neutral Fe core. These include: *s* electron, $h\nu+\text{Fe}^-([\text{Ar}]3d^74s^2\ ^4F)\rightarrow\text{Fe}([\text{Ar}]3d^74s\ ^5F,^3F)+e^-(kp)$, and *d* electron, $h\nu+\text{Fe}^-([\text{Ar}]3d^74s^2\ ^4F)\rightarrow\text{Fe}([\text{Ar}]3d^64s^2\ ^5D)+e^-(kp,kf)$, photodetachment channels. It should be noted that although the $^4F\rightarrow\ ^5P$ transition is energetically accessible, it is not allowed under conservation of orbital angular momentum selection rules for photodetachment. Shown in Fig. 6 are typical photoelectron kinetic energy spectra for the photodetachment of Fe^- at λ=457.9 nm and at polarization angles of $\theta=0°$ and 100°, respectively. In Fig. 7, the spectral dependence of photoelectron angular distributions are plotted

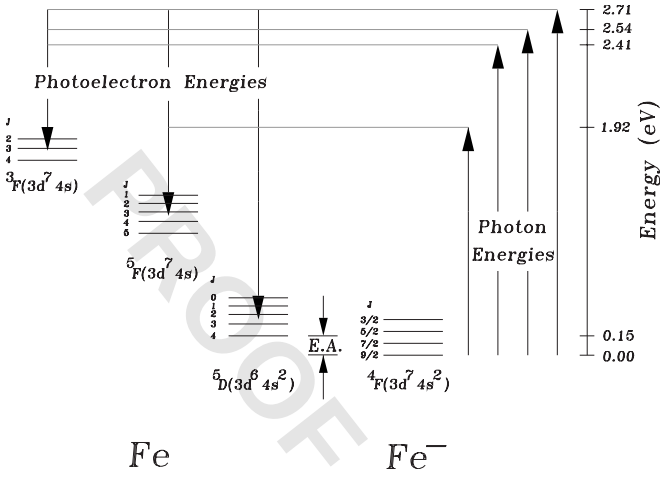

FIG. 5. A schematic energy level diagram for the photodetachment of Fe^- at visible photon energies.

for the ${}^4F \rightarrow {}^5D$, ${}^4F \rightarrow {}^5F$, and ${}^4F \rightarrow {}^3F$ transitions at all measured photoelectron kinetic energies. Here, the plotted values of the asymmetry parameter correspond to the weighted average of β between fine-structure states [see Eq. (6)], and the photoelectron kinetic energies were determined from the difference between incident photon energy and the peak centroid positions. The experimentally determined values of the asymmetry parameter for the single-photon detachment of

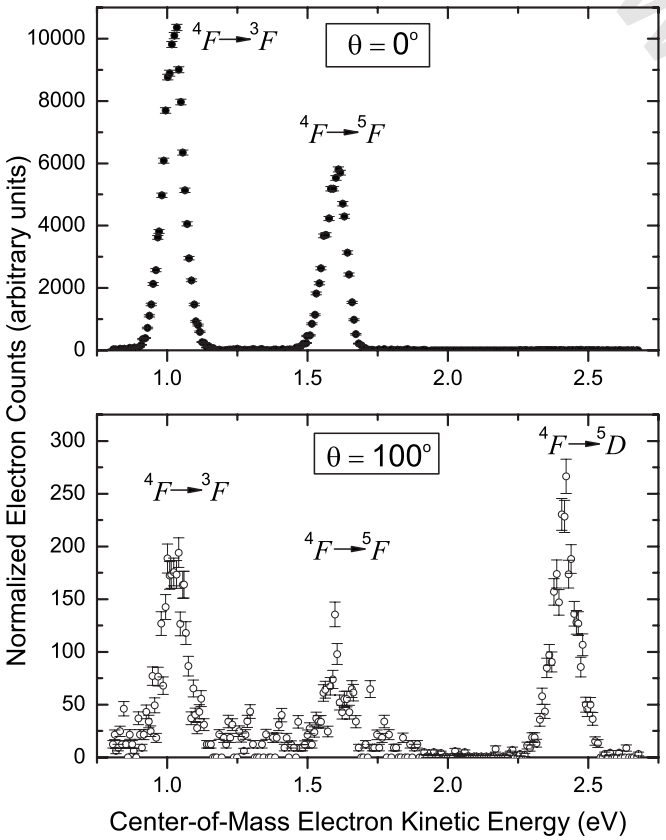

FIG. 6. Photoelectron kinetic energy spectra for the photodetachment of Fe^- at $\lambda = 457.9$ nm and at polarization angles of $\theta = 0°$ and 100°.

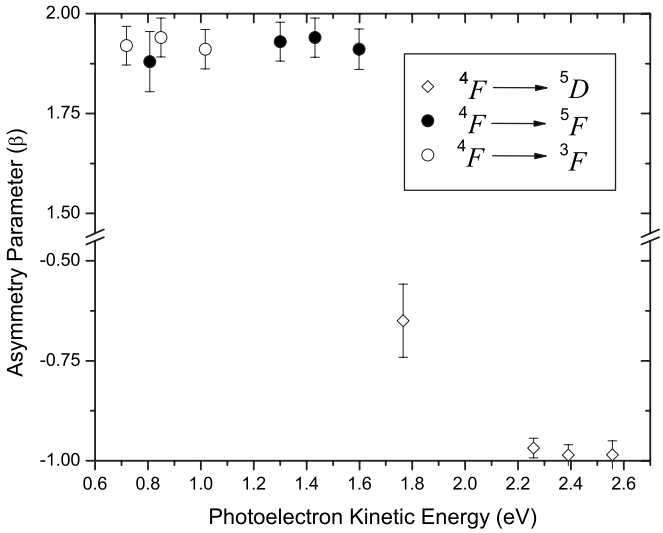

FIG. 7. A plot of asymmetry parameters versus center-of-mass photoelectron kinetic energies for all measured photon wavelengths for the ${}^4F \rightarrow {}^5D$ (◇), ${}^4F \rightarrow {}^5F$ (●), and ${}^4F \rightarrow {}^3F$ (○) Fe^- photodetachment channels. It is interesting to note that the asymmetry parameter value for the parity "unfavored" ${}^4F \rightarrow {}^5D$ transition near 1.8 eV is not $\beta = -1$, as would be expected from angular momentum transfer theory. Moreover, within experimental error bars shown to one standard deviation of the mean, the asymmetry parameters for s-electron detachment are not identically $\beta = 2$, as would be expected.

Fe^- for all observed photodetachment channels and at all measured wavelengths are given in Table II, along with their respective experimental uncertainties. The asymmetry parameters for photodetachment into F states shown in Table II are in excellent agreement with the values of $\beta \geq 1.9 \pm 0.1$ reported by Engelking and Lineberger [28] at a photon wavelength of 488.0 nm.

The description of the photodetachment of Fe^- must account not only for the relatively large numbers of different photodetachment channels that are energetically accessible, but also for the somewhat narrow photodetachment peaks, which show little or no spin-orbit structure at the experimen-

TABLE II. Asymmetry parameters for the photodetachment of Fe^- at visible photon wavelengths. The measured values of the asymmetry parameter are given for the single-photon detachment processes: $h\nu + Fe^-([Ar]3d^74s^2\ {}^4F) \rightarrow Fe([Ar]3d^74s\ {}^3F) + e^-$; $h\nu + Fe^-([Ar]3d^74s^2\ {}^4F) \rightarrow Fe([Ar]3d^74s^5F) + e^-$; and $h\nu + Fe^-([Ar]3d^74s^2\ {}^4F) \rightarrow Fe([Ar]3d^64s^{25}D) + e^-$.

Photon wavelength λ (nm)	Asymmetry parameter β_{exp}		
	${}^4F \rightarrow {}^3F$	${}^4F \rightarrow {}^5F$	${}^4F \rightarrow {}^5D$
647.1		1.88±0.08	−0.65±0.09
514.5	1.92±0.05	1.93±0.05	−0.97±0.03
488.0	1.94±0.05	1.94±0.05	$-0.99^{+0.03}_{-0.01}$
457.9	1.91±0.05	1.91±0.05	$-0.99^{+0.04}_{-0.01}$

TABLE III. Cross sections for the photodetachment of C^- from Ref. [5] and present results for Cu^- and Fe^- at discrete photon energies.

Photon wavelength λ (nm)	$\sigma(C^-)$ $^1S\rightarrow{}^2S$ (10^{-18} cm^2)	$\sigma(Cu^-)$ $^1S\rightarrow{}^2S$ (10^{-18} cm^2)	$\sigma(Fe^-)$ $^4F\rightarrow{}^3F$ (10^{-18} cm^2)	$\sigma(Fe^-)$ $^4F\rightarrow{}^5F$ (10^{-18} cm^2)	$\sigma(Fe^-)$ $^4F\rightarrow{}^5D$ (10^{-18} cm^2)
514.5	13.2±1.9	75±15	50±10	35±7	3.0±0.6
488.0	13.4±2.0	56±11	34±7	22±5	2.4±0.5

tal energy resolution achieved in these measurements. The source of these narrow peaks has been described as coming about due to a "nonstatistical" weighting of the J-component lines which comes about due to the triangle rule for total angular momentum coupling [28]. The source of these lineshapes is discussed in more detail in Sec. III E 2 below.

In Table II and Fig. 7, asymmetry parameter values for the $h\nu+\mathrm{Fe}^-(^4F)\rightarrow\mathrm{Fe}(^3F,^5F)+e^-$ photodetachment channels were shown to be significantly less than two within the experimental error. These results were unexpected since closed s-subshell photodetachment should lead to $\beta=2$. One can speculate that configuration interactions may play a relatively larger role in determining β values for s-subshell photodetachment for Fe^- than they do for Cu^- [15]. The energy dependence of the asymmetry parameter for the $\mathrm{Fe}^-(^4F)\rightarrow\mathrm{Fe}(^5D)$ photodetachment channel was shown to be dominated by parity "unfavored" values of the angular momentum transfer for photon energies $h\nu\geq 2.41$ eV. This result is in excellent agreement with the predicted values from angular momentum transfer theory [18]. However, at a photon energy of 1.92 eV, $\beta=-0.65\pm0.09$ for the $^4F\rightarrow{}^5D$ transition, which may also indicate that configuration interactions may be playing a larger role at photon energies closer to the photodetachment threshold.

D. Relative cross section measurements

Using dimensional analysis, the signal rate, $S(x)$, for the photodetachment into a channel x can be expressed as

$$S(x)=\frac{Y(x)}{T}=\frac{\sigma(x)}{4\pi}\{[1+\beta(x)P_2(\cos\theta)]\gamma\Phi k\rho(\Delta\Omega)V\}, \tag{10}$$

where $Y(x)$ is the photoelectron yield; T is the integration time; $\sigma(x)$ is the angular integral photodetachment cross section into channel x; $\beta(x)$ is the corresponding asymmetry parameter; $P_2(\cos\theta)$ is the second-order Legendre polynomial where θ is the angle between the linear polarization vector of photon beam and the momentum vector of the collected photoelectrons; $\Phi=[W/(A_L\cdot h\nu)]$ is the photon flux, where W is the laser power, A_L is the area of the laser beam, and $h\nu$ is the photon energy; k represents both the collection and detection efficiencies; $\rho=[I/(A_i\cdot v_i)]$ is the ion beam density where I is the ion beam current, A_i is the area of the ion beam, and v_i is the ion speed; $\Delta\Omega$is the solid angle defined by the collection geometry; V is the effective interaction volume between the beams; and γ is the frame-transformed solid angle ratio given in Eq. (9).

It is possible to obtain a relative measurement of an unknown photodetachment cross section $\sigma(x)$ by comparing the photoelectron yield of an unknown ion (Y_x) with the photoelectron yield (Y_r) of a reference ion for which the absolute cross section is known. With the highly stable, aperture limited, ion beams used in these measurements, the interaction volume between the ion and photon beams can be assumed to be constant $(V_x=V_r)$ since variations in the ion-photon beam overlap are negligible. Moreover, other parameters can be assumed to be constant as long as measurements are carried out using identical tuning conditions at the same photon energy. Included in these are the cross-sectional areas of the ion and laser beams and the detection efficiency. Using these assumptions and the expressions for the photon flux and ion beam density, the ratio of photodetachment cross sections is given by

$$\frac{\sigma(x)}{\sigma(r)}=\frac{Y_x}{Y_r}\frac{[1+\beta(r)P_2(\cos\theta_r)]}{[1+\beta(x)P_2(\cos\theta_x)]}\frac{\gamma_r W_r I_r v_x}{\gamma_x W_x I_x v_r}, \tag{11}$$

where θ_x and θ_r are polarization angles for the unknown and reference ions, respectively.

The results of photodetachment cross section measurements for Fe^-, C^-, and Cu^- at visible photon wavelengths are shown in Table III. The sources of experimental error for photodetachment cross section measurements are listed in Table IV using the Fe^- $(^4F\rightarrow{}^5F)$ transition as an example. The errors include contributions from measured parameters added in quadrature as well as the uncertainties in previously measured absolute photodetachment cross sections [5,6], which were added directly to determine the total uncertainty in the measured cross sections. At each discrete photon energy, 50 separate Fe electron energy spectra were collected and analyzed. Similar measurements were made on C^- and Cu^- before and after each Fe^- photoelectron energy spectrum was collected. Therefore, the ratio of photoelectron yields for two species for which absolute cross section measurements are known, i.e., C^- [5,29] and Cu^- [6], could be carried out under similar experimental conditions, providing a benchmark for the Fe^- measurements. A comparison of Cu^- photodetachment cross sections with previously measured and calculated cross sections is shown in Fig. 8. As is evident from Fig. 8, the present measurements are in very good agreement with the previous experimental results [6] and are consistent with the *ab initio* R-matrix values calculated by Scheibner and Hazi [2].

TABLE IV. Sources of experimental error in relative photodetachment cross section $\sigma(x)$ measurements for the Fe^- ($^4F \rightarrow {}^5F$) photodetachment channel estimated at 90% confidence level. The errors on the reference cross sections were added directly to the quadrature sum of relative and absolute errors.

Source of error	Uncertainties relative (%)	absolute (%)	total (%)
Electron counting statistics	4		4
Electron yield Y	2		2
Asymmetry parameter $\beta(x)$	2	2	3
Asymmetry parameter $\beta(r)$	2	2	3
Polarization angle θ	2	1	2
Solid angle ratio γ	3		3
Laser power W	3	2	4
Ion beam current I	2	2	3
Ion speed v_i	1	2	2
Quadrature sum	7	5	9
Reference cross section $\sigma(r)$			11
Total uncertainty in relative cross section $\sigma(x)$			20

E. Derived radiative electron attachment cross sections

The principle of detailed balance is based on the concept of microscopic reversibility for a two-body collision [30]. Using this principle, the equation for the radiative attachment cross section, σ_{ra}, can be derived from the experimentally measured cross section for photodetachment, σ_{pd}, using the following expression:

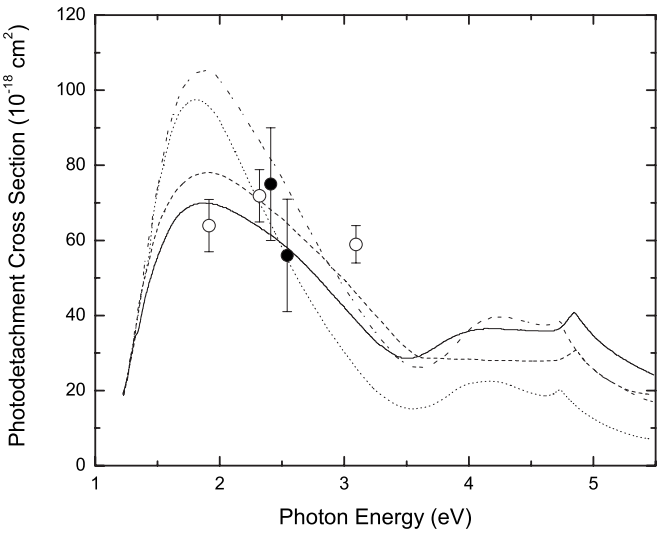

FIG. 8. A comparison of Cu^- photodetachment cross sections: The present experimental cross sections (●) are compared with the previous experimental values (○) of Balling *et al.* [6] and calculations of Scheibner and Hazi [2]. The curves represent two different *ab initio* *R*-matrix models in velocity and length form model B1: length form (–·–·–·–) and velocity form (·····), and model B2: length form (- - - - -) and velocity form (——).

TABLE V. Radiative attachment cross sections for Cu and Fe.

Photon wavelength λ (nm)	σ_{ra}(Cu) $^2S \rightarrow {}^1S$ (10^{-24} cm^2)	σ_{ra}(Fe) $^3F \rightarrow {}^4F$ (10^{-24} cm^2)	$^5F \rightarrow {}^4F$ (10^{-24} cm^2)	$^5D \rightarrow {}^4F$ (10^{-24} cm^2)
514.5	180±36	525±132	119±34	8.63±2.16
488.0	135±36	336±101	76±20	7.25±1.70

$$\sigma_{ra} = \left(\frac{g_{A^-}}{g_{A^0}}\right)\left(\frac{h}{\lambda}\right)^2\left(\frac{1}{2E_c m_e}\right)\sigma_{pd}. \quad (12)$$

In Eq. (12), λ is the wavelength of the incident photon, E_c is the center-of-mass kinetic energy of the liberated photoelectron, and g_{A^-} and g_{A^0} are the statistical weights of the atomic anion and resulting atomic neutral, respectively. For *LS* coupling, we can assume that $g=(2L+1)(2S+1)$ for the term ^{2S+1}L. The above equation can be recast in the following useful form:

$$\sigma_{ra} = \left(\frac{g_{A^-}}{g_{A^0}}\right)\left(\frac{6.626\times10^{-25}}{\lambda}\right)^2\left(\frac{3.42\times10^{48}}{E_c}\right)\sigma_{pd}, \quad (13)$$

where λ is in nm and E_c is in eV. One only need now enter λ, E_c, and σ_{pd}, all of which are known from the experiment, along with the statistical weights of the species in question into the above formula to calculate the radiative attachment cross section.

1. RA cross sections for Cu

For Cu, the center-of-mass photoelectron kinetic energies can be determined from Einstein's energy balance equation at a given photon wavelength (see Table I). Using these energies and the corresponding photodetachment cross sections and experimental uncertainties listed in Table III, the radiative attachment cross sections for Cu can be calculated via a substitution into Eq. (13). The calculated radiative attachment cross section values are listed in Table V.

2. RA cross sections for Fe

The determination of the radiative attachment cross sections for Fe are more complicated than those of Cu, since the Fe^- photoelectron kinetic energy spectra are not fine-structure resolved. Despite this, center-of-mass photoelectron kinetic energies can be determined from known energy levels for the energetically accessible ^5D, ^5F, and ^3F states of Fe I [31] and the tabulated fine structure levels of Fe^- [7]. Using this information, along with the wavelengths of the laser photons and the E_{EA} for Fe, one can calculate an estimated "weighted average" for the center-of-mass photoelectron kinetic energies for the states $^{2S+1}L_J$, assuming a statistical weighting of $(2J+1)$ for each $^{2S+1}L_J$ state. These estimated center-of-mass photoelectron kinetic energies can then be used, along with the other relevant experimental information listed in Table III, to calculate the radiative attachment cross section for Fe after substitution into Eq.(13). The calculated

radiative attachment cross sections for Fe are listed in Table V.

The relative intensities of the individual fine-structure photodetachment cross sectional line strengths for a single-photon, one-electron detachment from a negative ion can be calculated using the expression [28]

$$I(J_c,J_o) \sim (2J_c+1)(2J_o+1)\sum_{j=l-1/2}^{j=l+1/2}(2j+1)\begin{Bmatrix} S_o & L_o & J_o \\ \frac{1}{2} & l & j \\ S_c & L_c & J_c \end{Bmatrix}^2. \quad (14)$$

In Eq. (14), the line strengths are calculated for $J_o \rightarrow J_c$ transitions between *LS*-coupled states, and the spin, orbital, and total angular momentum quantum numbers of the initial Fe^- and neutral Fe core states, and photoelectron follow the convention described by the general PD process shown in Eq. (5). This expression is valid so long as the energy equivalent of the ion source temperature greatly exceeds the fine-structure splitting in Fe^-. This expression shows that the various fine-structure-resolved transitions do not occur with the $(2J_c+1)(2J_o+1)$ statistical weighting one might expect in a transition between two *LS*-coupled states. Instead, the intensity must take into account geometrical factors inherent in angular momentum coupling of the PD or RA processes. These geometrical factors are made manifest in Eq. (14) by the 9-*j* symbol, which imposes a triangular rule on the total angular momentum and tends to narrow the observed linewidths in the photoelectron kinetic energy spectra [28]. An example of calculated intensities for the $^4F \rightarrow {}^3F, {}^5F, {}^5D$ transitions is compared to experimental spectra in Fig. 9. In the figure, the experimental data (circles) were collected at the "magic" angle with a photon energy of 2.54 eV. The solid line in the figure represents a sum of Gaussian curves normalized to the experimental data. The fine-structure Gaussian line intensities (vertical lines) were calculated using Eq. (14) and the centroid locations were fixed to transition energies and the peak widths were fixed to those of Cu^- (see Fig. 3 above). There is good agreement between the measured and calculated Fe^- lineshapes for the $^4F \rightarrow {}^{3,5}F$ transitions, which display the "nonstatistical" narrowing of the overall linewidths reported by Engelking and Lineberger [28]. This result is expected since the *J* selection rules forced upon the $^4F \rightarrow {}^{3,5}F$ transitions, $|\Delta J| \leq \frac{1}{2}$, prohibit certain energetically allowed transitions. In contrast, the lineshape for the $^4F \rightarrow {}^5D$ transition (see inset Fig. 9) is narrower than expected. This is somewhat surprising since the selection rule imposed on this transition, $|\Delta J| \leq \frac{5}{2}$, indicates the peak should have been wider than what was actually measured in the experiment. Although the exact source of the narrowing of this transition is unknown, one can speculate that the configuration interaction may be limiting the validity of the *LS*-coupling approximation. This is consistent with the asymmetry parameter values for the $^4F \rightarrow {}^5D$ transition asymmetry parameters, which deviated considerably from the expected parity unfavored values of $\beta=-1$ (see Table II above).

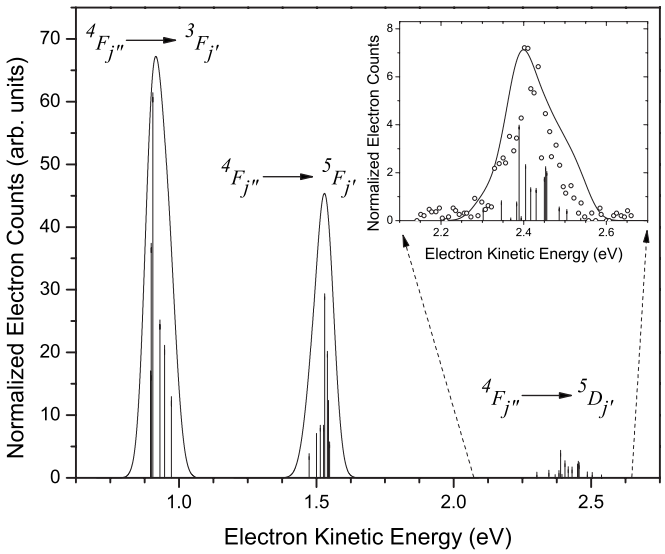

FIG. 9. Transitions for the photodetachment process $h\nu+Fe^- \rightarrow Fe+e^-$, taken at the "magic" angle ($\theta=54.74°$) with a photon wavelength of $\lambda=488.0$ nm. The hollow circles (○) are experimental data points, and the line through the circles is a superposition of Gaussian functions weighted according to the line strengths (vertical lines) determined via Eq. (14) for each fine structure allowed transition. The inset figure shows the $^4F_{J_o} \rightarrow {}^5D_{J_c}$ transitions on an expanded scale where the narrowing of the overall lineshape can be seen more clearly.

IV. CONCLUSION

Photodetachment cross sections for Cu^- and Fe^- have been measured at discrete visible photon wavelengths using the LPES technique. Photon-ion collision cross sections were determined by comparing the photoelectron yields from the photodetachment of Fe^- to anions with known absolute photodetachment cross sections. Using the measured photodetachment cross sections, radiative electron attachment cross sections for Cu and Fe were calculated using the principle of detailed balance.

Photoelectron angular distributions were mapped from laboratory frame, angle-, and energy-resolved measurements following the photodetachment of Cu^- and Fe^-, and values of the asymmetry parameters were obtained at several photon energies. The energy independence of the asymmetry parameter for the photodetachment process $h\nu+Cu^-([Ar]3d^{10}4s^{21}S) \rightarrow Cu([Ar]3d^{10}4s^2S)+e^-(kp)$ is clearly demonstrated in the experimental data, and is shown to be in excellent agreement with the predictions of models for closed *s*-subshell photodetachment [14,15]. In contrast, β values for the $h\nu+Fe^-([Ar]3d^74s^2\ ^4F) \rightarrow Fe([Ar]3d^74s^3F$ and $^5F)+e^-$ photodetachment channels were shown to be significantly less than two within the experimental error, leading to speculation that the configuration interaction plays a larger role in the *s*-electron photodetachment from a partially filled *s* subshell [15]. For photon energies $h\nu \geq 2.41$ eV, the spectral variation of the asymmetry parameter for the $Fe^-([Ar]3d^74s^2\ ^4F) \rightarrow Fe([Ar]3d^64s^2\ ^5D)$ photodetachment channel was shown to be dominated by parity "unfavored" values of the angular momentum transfer,

in agreement with the predicted values using the angular momentum transfer formalism of Fano and Dill [18]. However, at a photon energy of 1.92 eV, $\beta=-0.65\pm0.09$ for the $^4F\rightarrow{}^5D$ ground-state to ground-state channel, indicating that the configuration interaction may play a larger role at photon energies closer to the photodetachment threshold. Hopefully, these measurements will prove germane and stimulate further studies of these transition metal anions in basic atomic collision physics and low-temperature plasma environments.

ACKNOWLEDGMENTS

This work was made possible by the generous support of the US DOE under Grant No. DE-FC52-01NV14050 at UNR. We would like to thank the UNR physics department electrical and mechanical support staff including Bill Brinsmead, Wade Cline, Dennis Meredith, and Walt Weaver for technical support during these experiments.

[1] S. H. Massey, *Negative Ions*, 3rd ed. (Cambridge University Press, London, 1976).
[2] K. F. Scheibner and A. U. Hazi, Phys. Rev. A **38**, 539 (1988).
[3] A. Dalgarno, P. C. Stancil, and S. Lepp, Astrophys. Space Sci. **251**, 375 (1997).
[4] M. L. Seman and L. M. Branscomb, Phys. Rev. **125**, 1602 (1962).
[5] E. J. Robinson and S. Geltman, Phys. Rev. **153**, 4 (1967).
[6] P. Balling, C. Brink, T. Andersen, and H. K. Haugen, J. Phys. B **25**, L565 (1992).
[7] T. Andersen, H. K. Haugen, and H. Hotop, J. Phys. Chem. Ref. Data **28**, 1511 (1999).
[8] J. C. Rienstra-Kiracofe, G. S. Tschumper, H. F. Schaefer, S. Nandi, and G. B. Ellison, Chem. Rev. (Washington, D.C.) **102**, 231 (2002).
[9] V. T. Davis, J. Ashokkumar, and J. S. Thompson, Phys. Rev. A **65**, 024702 (2002).
[10] D. Calabrese, A. M. Covington, W. W. Williams, D. L. Carpenter, J. S. Thompson, and T. J. Kvale, Phys. Rev. A **71**, 042708 (2005).
[11] T. Andersen, Phys. Rep. **394**, 157 (2004).
[12] D. J. Pegg, Rep. Prog. Phys. **67**, 857 (2004).
[13] C. N. Yang, Phys. Rev. **74**, 764 (1948).
[14] J. Cooper and R. N. Zare, J. Chem. Phys. **48**, 942 (1968).
[15] S. T. Manson and A. F. Starace, Rev. Mod. Phys. **54**, 389 (1982).
[16] D. Dill, Phys. Rev. A **7**, 1976 (1973).
[17] U. Fano, Phys. Rev. **124**, 1866 (1961).
[18] U. Fano and D. Dill, Phys. Rev. A **6**, 185 (1972).
[19] G. D. Alton, Nucl. Instrum. Methods Phys. Res. A **244**, 142 (1986).
[20] G. D. Alton, Nucl. Instrum. Methods Phys. Res. B **73**, 221 (1993).
[21] D. Calabrese, A. M. Covington, D. L. Carpenter, J. S. Thompson, T. J. Kvale, and R. Collier, J. Phys. B **30**, 4791 (1997).
[22] A. M. Covington, D. Calabrese, W. W. Williams, J. S. Thompson, and T. J. Kvale, Phys. Rev. A **56**, 4746 (1997).
[23] N. Stolterfoht, Phys. Rep. **146**, 317 (1987).
[24] R. C. Bilodeau, M. Scheer, and H. K. Haugen, J. Phys. B **31**, 3885 (1998).
[25] *CRC Handbook of Chemistry and Physics*, 73rd ed., edited by D. R. Lide (CRC Press, Ann Arbor, MI, 1992).
[26] H. Hotop, J. Chem. Phys. **58**, 2373 (1973).
[27] D. G. Leopold and W. C. Lineberger, J. Chem. Phys. **85**, 51 (1986).
[28] P. C. Engelking and W. C. Lineberger, Phys. Rev. A **19**, 149 (1979).
[29] C. A. Ramsbottom, K. L. Bell, and K. A. Berrington, J. Phys. B **26**, 4399 (1993).
[30] E. W. McDaniel, *Atomic Collisions, Electron and Photon Projectiles* (Wiley, New York, 1989).
[31] Y. Ralchenko, F. C. Jou, D. E. Kelleher, A. E. Kramida, A. Musgrove, J. Reader, W. L. Wiese, and K. Olsen, NIST Atomic Spectra Database (version 3.1.0) (2006), http://physics.nist.gov/PhysRefData/ASD/index.html.